Two-Phase Spray Cooling of Hybrid Vehicle Electronics

Issam Mudawar, Desikan Bharathan, Kenneth Kelly, and Sreekant Narumanchi

***Abstract*—As part of the U.S. Department of Energy's (DOE's) Power Electronics and Electric Machines program area, the DOE's National Renewable Energy Laboratory (NREL) is currently leading a national effort to develop next-generation cooling technologies for hybrid vehicle electronics. Spray cooling has been identified as a potential solution that can dissipate 150–200 W/cm^2 while maintaining the chip temperature below 125 °C. This paper explores the viability and implementation of this cooling scheme. First, commercial coolants are assessed for their suitability to this application in terms of thermal, environmental, and safety concerns and material compatibility. In this assessment, HFE-7100 is identified as the optimum coolant in all performance categories. Next, spray models are used to determine the HFE-7100 spray conditions that meet such stringent heat dissipation requirements. These findings are verified experimentally, demonstrating that spray cooling is a viable thermal management solution for hybrid vehicle electronics.**

***Index Terms*—Boiling, critical heat flux (CHF), dielectric coolant, hybrid vehicles, phase change, power electronics, refrigerant, sprays.**

I. Nomenclature

A, A'	Area.
B	Nucleate boiling coefficient.
Bo	Boiling number.
c_p	Specific heat.
d_{32}	Sauter mean diameter (SMD).
d_o	Nozzle orifice diameter.
H	Orifice-to-surface distance.
h_{fg}	Latent heat of vaporization.
k	Thermal conductivity.
L	Length and width of square test surface.
P	Pressure.
ΔP	Pressure drop across spray nozzle.
Pr	Prandtl number.
$P_{\rm sat}$	Saturation pressure.
Q	Volumetric flow rate.
Q''	Local volumetric spray flux.
$\overline{Q''}$	Average volumetric spray flux based on circular impact area of spray.
q''_m	Average critical heat flux based on total area of square surface.
$\mathrm{q}''_{m,p}$	Local critical heat flux.
q''_s	Device heat flux.
r	Radial distance from centerline of spray.
Re_{d_0}	Reynolds number based on nozzle orifice diameter.
T	Temperature.
T_f	Nozzle inlet temperature.
T_s	Surface temperature.
$T_{\rm sat}$	Saturation temperature.
$\Delta T_{\rm sub}$	Difference between saturation temperature and nozzle inlet temperature $T_{\rm sat} - T_f$.
We_{d_0}	Weber number based on nozzle orifice diameter.

Greek Symbols:

γ	Angular coordinate in volumetric flux model.
θ	Spray cone angle.
μ	Viscosity.
ρ	Density.
σ	Surface tension.

Subscripts:

d_o	Dameter of nozzle orifice.
f	Liquid; nozzle inlet.
g	Vapor.
m	Maximum critical heat flux (CHF).
p	Point-based.
s	Surface.
sat	Saturation.
sub	Subcooling.

Manuscript received April 04, 2008. First published February 06, 2009; current version published July 22, 2009. This work was supported by the National Renewable Energy Laboratory under Subcontract YEV-6-55511-01 under the U.S. Department of Energy Contract DE-AC36-99GO10337. This work was recommended for publication by Associate Editor M. Arik upon evaluation of the reviewers comments.

I. Mudawar is with the Mudawar Thermal Systems, West Lafayette, IN 47906 USA (e-mail: im@mudawar.com).

D. Bharathan, K. Kelly, and S. Narumanchi are with the National Renewable Energy Laboratory, Golden, CO 80401 USA.

Digital Object Identifier 10.1109/TCAPT.2008.2006907

II. Introduction

A. Near-Term and Long-Term Transitions in Vehicle Technology

ACHIEVING energy independence ultimately depends on successfully developing hybrid electric and fuel cell vehicles that are economically justifiable to the average consumer.

This will require reducing the production cost of current automotive electric traction systems by a factor of four. Thus, the size of the systems will have to be reduced by more than 50%, and greater modularity will be needed to support increases in system configurations and economies of scale [1]. For the technology to be successfully adopted, system integration will also be essential to reduce the part count and to improve reliability, durability, and producibility.

In recent years, we have witnessed unprecedented interest in the development of a new electric propulsion system to facilitate the transitioning from conventional engines to economical combustion engine hybrid vehicles in the near term and to fuel cell vehicles in the long term. To achieve these goals, a major collaborative effort was launched through the FreedomCAR and Fuel Partnership, which include the U.S. Department of Energy (DOE), BP America, Chevron Corporation, ConocoPhillips, Exxon Mobil Corporation, Shell Hydrogen LLC, and the United States Council for Automotive Research, a legal partnership among Chrysler LLC, Ford Motor Company, and General Motors Corporation [1].

Interestingly, electrical propulsion systems are already available in the market, but their use is hindered by their cost-about $33/kW, which amounts to $1815 for a complete 55-kW system [1]. The goal, then, in developing new electric propulsion systems is to decrease their cost to a level that renders hybrid and fuel cell vehicles economically justifiable for consumers. As shown in Fig. 1, the DOE's target is to reduce the cost of an electric propulsion system (which includes an electric traction motor, inverter, and voltage booster) to $12/kW by 2015 and $8/kW by 2020. This would bring the total cost of the system to $660 by 2015 and $440 by 2020.

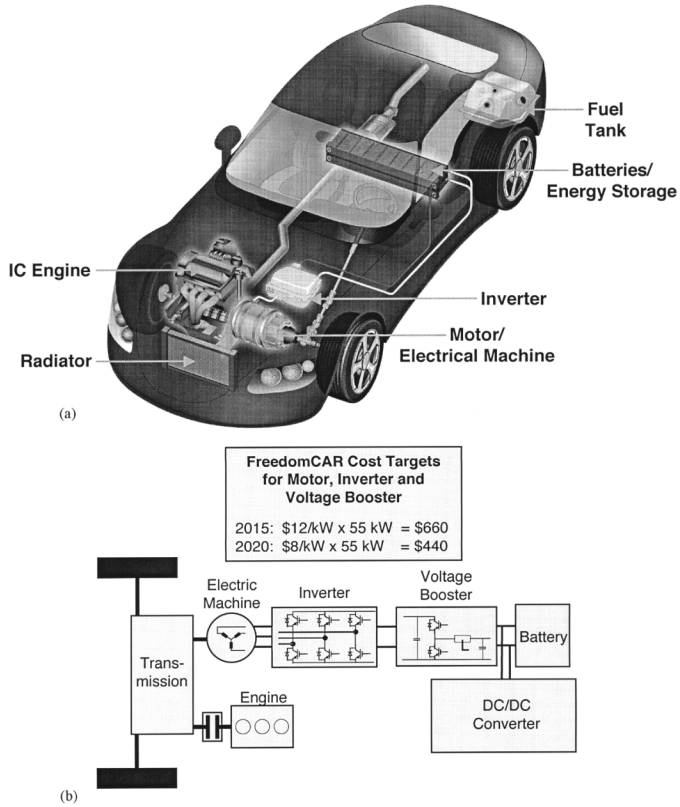

Fig. 1. (a) Propulsion system components for hybrid vehicle. (b) Parallel hybrid vehicle configuration (adapted from [2]) and FreedomCAR cost targets [1].

B. Role of Thermal Management

To successfully integrate power electronics and electric machines into an electronics system, various thermal characteristics and performance targets must be met along with reducing the weight, volume, and cost of the electronic components. Thermal management plays a vital role in the pursuit of these goals.

The National Renewable Energy Laboratory (NREL) currently leads research and development activities in thermal control as part of the DOE Vehicle Technologies Program's Power Electronics and Electrical Machines activities. The overall objective of the thermal control activities is to develop advanced technologies and effective integrated thermal control systems that meet DOE program goals. The following are some key barriers in the development of thermal control technologies:

- Existing thermal control techniques are not adequate for dissipating high heat fluxes while limiting the operation of silicon-based electronic components to a temperature of less than 125 °C.
- Current components are generally both bulky and heavy, resulting in the need for additional structural support and increased use of parasitic power.
- Material and processing technologies remain too costly for use in the automotive industry.

To reach the DOE program goals, significant advances must be achieved in the thermal control of both the power electronics and motors. By optimizing existing technologies and extending them to new pioneering cooling methods, NREL aims to achieve higher power densities, smaller volumes and weights, and increased reliability for the drivetrain components. These efforts will also lead to lower costs for the new technologies, so they can be implemented in the automotive industry.

The current study was performed by a partnership consisting of Mudawar Thermal Systems, Inc., under a subcontract from NREL, and NREL to develop advanced thermal management solutions that utilize spray cooling *to dissipate* 150–200 W/cm^2 *from silicon-based electronic devices in hybrid vehicles while maintaining the device temperature below* 125 °C. While the use of trench insulated-gate bipolar transistors (IGBTs), which are silicon-based and can withstand up to 150 °C, is becoming more prevalent in inverters, the use of a lower maximum temperature of 125 °C was deemed more appropriate for thermal management system design.

III. Selecting a Thermal Management Solution

A. Direct Versus Indirect Liquid Cooling

Achieving the aforementioned heat flux dissipation and device temperature is highly dependent on chip packaging. Virtually all existing hybrid vehicle cooling work centers on *indirect liquid cooling* of the chip as illustrated in Fig. 2(a). Cooling performance in this case is only partially dictated by the convective

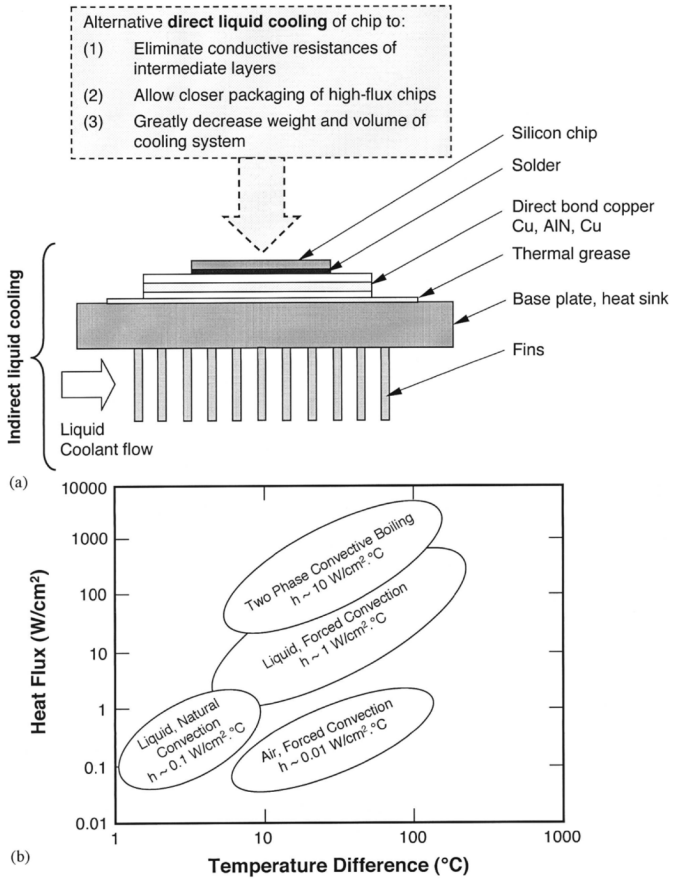

Fig. 2. (a) Cooling path for removing heat from silicon die using indirect cooling with water/ethylene glycol, and alternative direct liquid cooling. (b) Capabilities of existing cooling technologies using various fluids and operating pressures.

boundary. Because of the resistances of the different layers of materials separating the chip from the liquid coolant, a relatively large temperature gradient is incurred when dissipating high heat fluxes. These resistances may be completely eliminated by *direct liquid cooling* of the chip. However, having liquid come in direct contact with the chip's surface limits cooling options to a few dielectric and inert coolants. Unfortunately, the thermophysical properties of these coolants are quite inferior to those of common coolants such as water/ethylene glycol. Direct liquid cooling is therefore advantageous only when its convective thermal resistance is smaller than the sum of the convective, conductive and contact resistances of the indirect cooling configuration illustrated in Fig. 2(a). Because heat spreading plays a minor role in a direct cooling system, high-flux chips may be packaged quite close to one another, greatly reducing both the weight and the volume of the cooling system.

Given the inferior thermophysical properties of dielectric coolants and the strong dependence of cooling performance on convective resistance, the viability of a direct cooling system is highly dependent on the ability to achieve very large convective heat transfer coefficients. As shown in Fig. 2(b), this goal can be realized by adopting a highly effective liquid cooling configuration (e.g., spray, jet impingement, microchannel flow) and also by capitalizing on the benefits of phase change.

The primary objective of this study is to explore the effectiveness of direct two-phase spray cooling in meeting the heat flux and temperature requirements of future hybrid vehicle electronics.

B. Spray Cooling

High-flux electronic cooling applications demand the use of specialized types of sprays-pressure sprays-that utilize liquid momentum rather than a secondary air stream to break up the liquid into fine droplets. A large increase in the liquid's surface-area-to-volume ratio is achieved that, coupled with the broad dispersion of droplets across the heat-dissipating surface, both increases the spray's convective high heat transfer coefficient and helps to ensure the surface temperature uniformity demanded by electronic devices [3].

Toda [4] observed that subcooling the spray liquid had minor effects on single-phase and nucleate boiling heat transfer and did not have a dominant effect on critical heat flux (CHF). Both Toda [4] and Monde [5] showed that spray volumetric flux Q'' has by far the strongest effect on cooling performance. Volumetric flux is defined as the flow rate of spray liquid impacting an infinitesimal portion of the surface divided by the area of the same portion; it has the units of velocity.

Cho and Wu [6] developed a CHF correlation for Freon-113 sprays based on Weber number but did not account for droplet size. Mudawar and Valentine [7] determined local cooling characteristics for all regimes of the boiling curve for water. Like Toda and Monde, they showed that volumetric flux had the most dominant effect on spray cooling. Estes and Mudawar [8] developed an empirical relation for CHF for FC-72, FC-87 and water based on local volumetric flux Q'' and Sauter mean diameter (SMD) d_{32} but not droplet speed. However, Chen *et al.* [9] concluded that d_{32} has a negligible effect on CHF, while droplet velocity is a dominant parameter in the determination of CHF.

There are many barriers to implementing sprays to cool high-flux electronic devices. These barriers stem mostly from a poor understanding of spray cooling compared with competing options such as jet-impingement. There are also practical concerns resulting from the lack of repeatability of cooling performance for seemingly identical nozzles because of minute manufacturing imperfections or due to corrosion or erosion of the nozzle's interior passages [10].

C. Cooling Loop Options

Two different cooling loop configurations are considered for possible implementation of spray cooling. As shown in Fig. 3(a), the first consists of modifying the vehicle's refrigeration loop with a pump-assisted sub-loop containing a spray-cooling chamber in which the heat is removed from the vehicle electronics. Fig. 3(b) shows an alternative configuration, in which the electronics are cooled by a separate loop using an appropriate coolant.

The modified refrigeration loop configuration requires using the same coolant currently employed in the primary loop R134a. Pressure in this loop is set at about 2069 kPa (300 psia) and the coolant temperature at the saturation temperature for R134a corresponds to the same pressure. With a separate loop, there is far greater flexibility in selecting the coolant, operating pressure

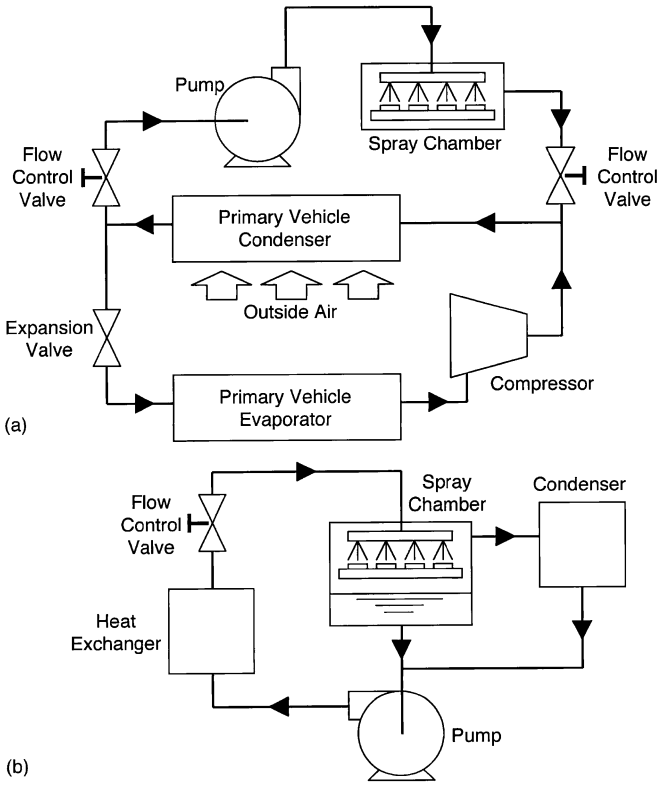

Fig. 3. Cooling of hybrid vehicle power electronics by (a) modifying existing R134a air-conditioning refrigeration loop and (b) using a separate cooling loop with appropriate coolant.

and, hence, coolant temperature. However, a maximum pressure of about 2069 kPa (300 psia) is desired for the separate loop as well to preclude excessive system weight. The pressure must also be maintained above ambient to prevent air inclusion in the event of a system leak. Such an inclusion can lead to a substantial deterioration in the condenser's performance as well as induce cavitation inside the pump.

Other important parameters concern the spray chamber itself. The primary heat dissipation requirement is to remove 150–200 W/cm^2 while maintaining the chip temperature below 125 °C.

With a typical device-to-coolant temperature drop of about 30 °C in the nucleate boiling regime for spray cooling [8], the coolant temperature should be maintained below 95 °C. Since the saturation temperature is the highest possible coolant temperature for a coolant intended for phase-change cooling, we can conclude that the saturation temperature of the coolant corresponding to the spray chamber pressure should be below 95 °C as well.

Another temperature limit concerns the condenser. As a result of phase change, the coolant temperature inside the condenser remains close to the saturation temperature as the vapor is gradually converted to liquid. The condenser is cooled externally by ambient air. Recent calculations at NREL reveal that the log-mean temperature difference between the coolant and air is about 30 °C. For a relatively high ambient air temperature of 30 °C, this implies that the coolant saturation temperature in the condenser must be no less than 60 °C. Therefore, the saturation temperature in the separate loop must satisfy the criterion $60 < T_{\rm sat} < 95$ °C and the pressure must be maintained in the range of 101.3–2069 kPa (14.7–300 psia).

D. Coolant Selection

Thermal requirements represent only one aspect of the task of selecting an appropriate coolant. Other crucial requirements include high dielectric strength, inertness and material compatibility, safety, and environmental concerns. Two different types of coolant are considered, refrigerants and liquid coolants; the latter are fluids that maintain a liquid state at atmospheric pressure. Both types of coolants are examined based on the following criteria.

- *Dielectric strength:* The highest voltage that can be sustained across a layer of the fluid before fluid breakdown or arcing takes place.
- *Dielectric constant*: The amount of electrostatic energy that can be stored per unit volume of fluid when a unit voltage is applied.
- *Flammability*: The susceptibility of the fluid to ignite, either spontaneously or as a result of a spark or open flame.
- *Auto-ignition temperature*: The temperature at which fluid would self-ignite.
- *Lower explosive limit* (LEL): The concentration of fluid for a given volume of air that renders a mixture flammable or explosive.
- *Atmospheric lifetime*: The time required for fluid concentration in the atmosphere to drop to $1/e$ of its initial value.
- *Ozone depletion potential* (ODP): A relative index indicating the extent to which the fluid may cause ozone depletion; the highest value, 1.0, is assigned to the highly ozone-depleting R11.
- *Global warming potential* (GWP): Indicates how much a given mass of the refrigerant contributes to global warming over a 100-year period compared with the same mass of CO_2; the latter is assigned a GWP value of 1.0.

A recent comprehensive study [11] grouped these performance criteria into general categories, including environmental, safety, dielectric strength, and material compatibility. The environmental rating is based on ODP and GWP. A *good* rating corresponds to zero ODP *and* a GWP of less than 1500, an *average* rating indicates $0.1 > \text{ODP} > 0$ *or* $6000 > \text{GWP} > 1500$, and a *poor* rating indicates $\text{ODP} > 0.1$ *or* $\text{GWP} > 6000$. The safety rating is based on flammability. A coolant is rated *good* if it is nonflammable and *poor* if it is flammable.

There are three main families of refrigerants. The earliest to be introduced were chlorofluorocarbons (CFCs) (e.g., R11, R12, R113, and R114), which are composed of chlorine, fluorine and carbon. While CFCs are both nontoxic and inert, they are highly ozone-depleting and contribute to global warming. Hydrochlorofluorocarbons (HCFCs) (e.g., R123, R124, and R141b) constitute a more recent alternative to CFCs, given their somewhat similar inertness and cooling characteristics but less than 10% of the ozone-depleting effects of CFCs. More recently, a new family of refrigerants, hydrofluorocarbons (HFCs) (e.g., R134a and R143a) have been introduced that provide essentially zero ozone depletion and reduced global warming effects.

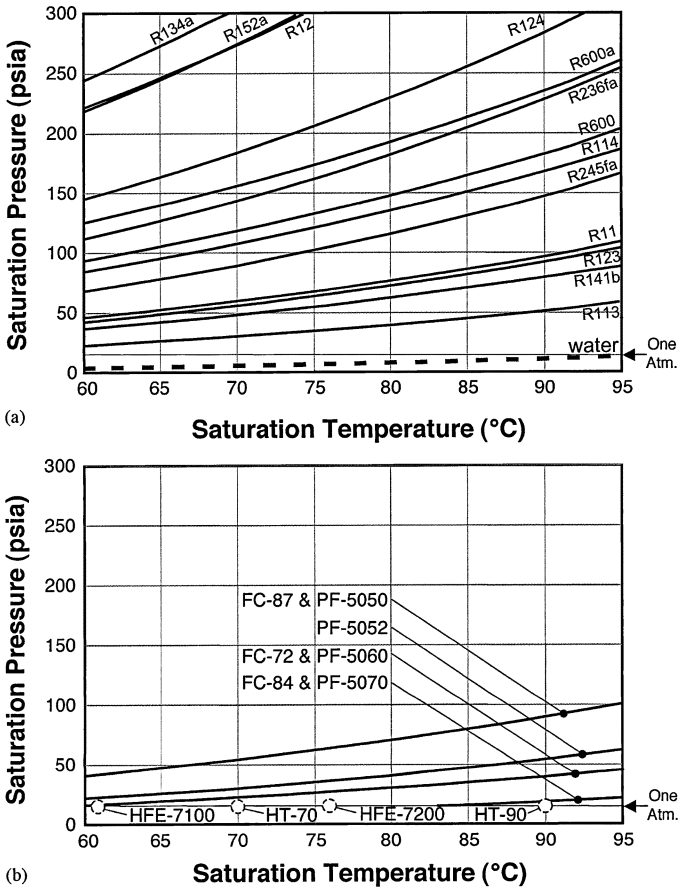

Fig. 4. Pressure-temperature saturation characteristics for (a) refrigerants and (b) liquid coolants (characteristics for some of the liquids are available over the entire temperature range; for others, saturation temperatures are available only at one atmosphere).

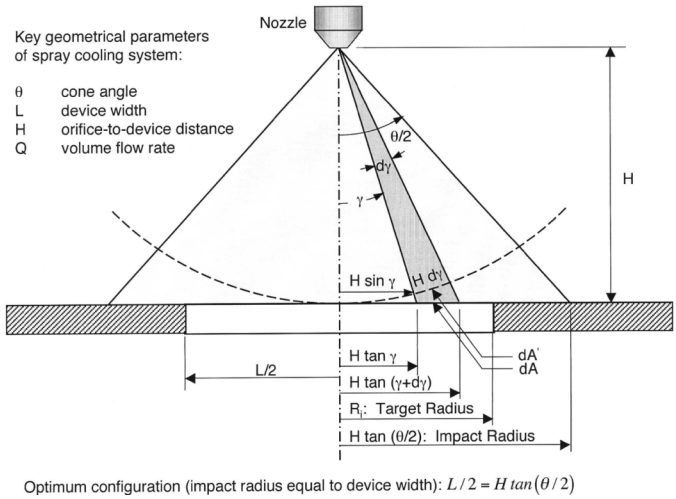

Fig. 5. Point-source model of volumetric flux distribution for pressure spray nozzle.

As discussed earlier, the desired operating saturation pressure-temperature $(P_{\rm sat} - T_{\rm sat})$ plane is 101.3–2069 kPa (14.7–300 psia) and 60 °C–95 °C, respectively. Fig. 4(a) shows that 13 of the refrigerants fall in the desired $P_{\rm sat} - T_{\rm sat}$ plane. Four of these (R141b, R152a, R600, and R600a) have *poor* safety ratings because of their flammability. All remaining nine refrigerants have *good* ratings in this category. Four CFCs (R11, R113, R114, and R12) and one HFC (R236fa) have *poor* ratings in the environmental category and have already been phased out by the Montreal Protocol because of their high ODP [12]. In contrast, R236fa has zero ODP but very high GWP. All three HCFCs (R123, R124, and R141b) in Fig. 3(a) have *average* environmental ratings because of their nonzero ODP. Refrigerants with *good* environmental ratings include two HFCs (R134a and R245fa) and two hydrocarbons (R600 and R600a). Overall, only R134a and R245fa have received good ratings in most categories. Of these two, only R134a has complete published thermophysical properties.

A similar fluid assessment was conducted for liquid coolants [11]. These include the following families of fluids: 3M Fluorinert (FCs), 3M Novec (HFCs), 3M Performance (FCs), Certonal, Solvay HT and ZT, Cooper Environtemp and Tranelec, Paratherm NF, Dow Corning OS-120, and Intech EDM. A key obstacle in using many of these coolants is the shortage of thermophysical property data; only 3M fluids come with detailed property information. The 3M coolants include perfluorocarbons (PFCs) (Fluorinerts FC-72, FC-87 and FC-84, and Performance Fluids PF-5050, PF-5052, PF-5060 and PF-5070), and HFCs (Novec fluids HFE-7100 and HFE-7200).

Fig. 4(b) shows that 12 of the 3M liquid coolants fall in the desired $P_{\rm sat} - T_{\rm sat}$ plane. All 3M liquid coolants have *good* safety ratings, though HFE-7200 carries a low LEL. However, Fluorinerts (FC-72, FC84, FC-87) and Performance Fluids (PF-5050, PF-5052, PF-5060 and PF-5070) have only *average* environmental ratings because of their relatively high GWP. Overall, only HFE-7100 has *good* ratings in all performance categories. It is important to note that the freeze point for HFE-7100 is −135 °C, which is well below any expected automobile application range of temperatures down to −40 °C.

Based on this coolant assessment study, one refrigerant, R134a, and one liquid coolant, HFE-7100, are deemed suitable for cooling hybrid vehicle electronics. In the following section, we consider the spray cooling performance of these two coolants.

IV. Spray Cooling Performance Predictions

A. Spray Configuration and Predictive Relations

Two spray parameters have significant influence on nucleate boiling heat transfer performance and CHF: volumetric flux, Q'', and Sauter mean diameter, d_{32}. While d_{32} is fairly uniform across the spray, Q'' for full-cone spray nozzles (which are favored for electronic cooling applications) exhibits significant spatial variations.

Mudawar and Estes [13] provided a detailed study of the spatial variation of volumetric flux for a full-cone spray nozzle. They modeled the nozzle orifice as a uniform point source for fluid flow. Fig. 5 shows that a constant volumetric flux along a spherical surface of radius equal to the orifice-to-surface distance would yield a nonuniform volumetric flux distribution

along the heated surface. The model yielded the following expression for local volumetric flux Q'' along the heated surface:

$$\frac{Q''}{\bar{Q}''} = \frac{1}{2}\left[\frac{\tan^2(\theta/2)}{1-\cos(\theta/2)}\right]\frac{1}{\left[1+\left(\frac{\mathrm{r}}{\mathrm{H}}\right)^2\right]^{3/2}} \tag{1}$$

where $\bar{Q}''$ is the mean volumetric flux across the impact area

$$\bar{Q}'' = \frac{Q}{\pi\{H\tan(\theta/2)\}^2}. \tag{2}$$

This model predicts a higher flow rate at the center of the spray impact area in comparison to the circumference of the same area. The spatial variations of Q'' have a strong bearing on both cooling uniformity and CHF. The relatively low volumetric flux in the outer regions means that CHF would commence at the circumference. Mudawar and Estes [13] demonstrated experimentally how a large orifice-to-surface distance causes a significant portion of the spray droplets to fall outside of the heated area. Conversely, a small distance results in a small droplet impact area, depriving much of the heated test surface of the advantages of direct droplet impact. Both extremes yield relatively low CHF values, and *CHF is highest when the impact area just inscribes the square heated surface*, i.e., when

$$H\tan(\theta/2) = L/2 \tag{3}$$

and

$$\bar{Q}'' = Q/(\pi L^2/4). \tag{4}$$

Estes and Mudawar [8] used the orifice diameter d_o and liquid velocity at the orifice $(2\Delta P/\rho_f)^{0.5}$ to represent the characteristic length and velocity, respectively, for full cone spray nozzles. They correlated Sauter mean diameter data for FC-72, FC-87 and water according to the relation

$$\frac{d_{32}}{d_0} = 3.67\left[\mathrm{We}_{d_0}^{1/2}\mathrm{Re}_{d_0}\right]^{-0.259} \tag{5}$$

where We_{do} and Re_{do} are defined, respectively, as

$$We_{d_o} = \frac{\rho_g(2\Delta P/\rho_f)d_o}{\sigma} \tag{6}$$

and

$$Re_{d_o} = \frac{\rho_f(2\Delta P/\rho_f)^{1/2}d_o}{\mu_f}. \tag{7}$$

Recently, Rybicki and Mudawar [14] combined their upward-oriented PF-5052 spray data with the downward-oriented water spray data of Mudawar and Valentine [7] to derive the following nucleate boiling correlation

$$Bo^* = 4.79\times10^{-3}\left(\frac{c_{p,f}(T_s-T_f)}{h_{fg}}\right)^{5.75} \tag{8}$$

where

$$Bo^* = \frac{\left(\frac{q_s''d_{32}}{\mu_f h_{fg}}\right)}{\left(\frac{\rho_f}{\rho_g}\right)^{2.5}\left(\frac{\rho_f\overline{Q}''^2d_{32}}{\sigma}\right)^{0.35}}. \tag{9}$$

Using their data for FC-72 and FC-87 along with Mudawar and Valentine's [7] water data, Estes and Mudawar [8] developed the following correlation for *local* CHF along the outer edge of the impact area, $q''_{m,p}$, based on volumetric spray flux along the same edge:

$$\frac{q''_{m,p}}{\rho_g h_{fg}Q''} = 2.3\left(\frac{\rho_f}{\rho_g}\right)^{0.3}\left(\frac{\rho_f Q''^2 d_{32}}{\sigma}\right)^{-0.35} \times\left(1+0.0019\frac{\rho_f c_{p,f}\Delta T_{\mathrm{sub}}}{\rho_g h_{fg}}\right). \tag{10}$$

Equation (10) can be used to determine the measured CHF data (based on the total area of a square test surface) in terms of the mean volumetric flux according to the following transformation:

$$q''_{m,p} = q''_m\frac{L^2}{\left(\frac{\pi}{4}L^2\right)} = \frac{4}{\pi}q''_m \tag{11}$$

and

$$\frac{Q''}{\overline{Q''}} = \frac{1}{2}\{1+\cos(\theta/2)\}\cos(\theta/2). \tag{12}$$

Equation (12) is derived by substituting $r = H\tan(\theta/2)$ in (1).

B. Predictions

As indicated earlier, only conditions falling in the pressure range of one atmosphere to $P_{\mathrm{sat}} = 2069$ kPa (300 psi) and saturation temperature range of $T_{\mathrm{sat}} = 60$ °C–95 °C are considered for the hybrid vehicle application. To achieve temperatures in excess of 60 °C with R134a, high pressures between 1700 and 2067 kPa are required. As shown in Table 1, the corresponding saturation temperature range is fairly narrow, between 60 °C and 68.9 °C. Thus, two representative temperatures are examined for R134a, one corresponding to each limit of this temperature range. Table I provides all relevant thermophysical properties corresponding to these temperatures.

As shown in Table I, HFE-7100 provides a fairly broad range of saturation temperatures, from $T_{\mathrm{sat}} = 60.4$ °C at one atmosphere to $T_{\mathrm{sat}} = 95.0$ °C corresponding to a pressure of 275.9 kPa. In other words, this coolant spans virtually the entire operating temperature range for hybrid vehicles at moderate to mild operating pressures. Five representative temperatures are examined for this coolant, spanning the range of 60.4 °C to 95 °C. Table I provides all relevant thermophysical properties corresponding to these temperatures.

The spray cooling relations discussed in the previous section are used to predict the cooling performances of three full-cone spray nozzles used in previous studies by Mudawar and Estes [13] and Rybicki and Mudawar [14]. Table II provides values for orifice diameter d_o and spray angle θ for each of these nozzles.

The thermal performance results for R134a and HFE-7100 are presented in the form of (1) the relationship between heat flux q''_s and surface temperature T_s in the nucleate boiling regime and (2) CHF value. Notice that the relationship between q''_s and T_s, which is given by (8) and (9), can be expressed for a given nozzle at each saturation temperature and flow rate as

$$q''_s = B(T_s - T_f)^{5.75}. \tag{13}$$

TABLE I
OPERATING CONDITIONS AND CORRESPONDING THERMOPHYSICAL PROPERTIES USED IN THERMAL ANALYSIS

Spray chamber constraints: $60 < T_{sat} < 95$ °C & $101.3 < P_{sat} < 2069$ kPa

R134a				
Sat. Pressure P_{sat} (kPa)	Sat. Temp. T_{sat} (°C)	Latent Heat of Vap. h_{fg} (kJ/kg)	Liquid Specific Heat $c_{p,f}$ (kJ/kg.K)	Liquid Density ρ_f (kg/m^3)
1700	60.0	138.8	1.669	1052
2069	68.9	126.0	1.791	1002
Vapor Density ρ_g (kg/m^3)	Liquid Viscosity μ_f (kg/m.s)	Liquid Thermal Conduct. k_f (W/m.K)	Liquid Prandtl Number Pr_f	Surface Tension σ (N/m)
88.69	0.000124	0.0647	3.18	0.0037
112.67	0.000109	0.0594	3.27	0.0027

a

HFE-7100				
Sat. Pressure P_{sat} (kPa)	Sat. Temp. T_{sat} (°C)	Latent Heat of Vap. h_{fg} (kJ/kg)	Liquid Specific Heat $c_{p,f}$ (kJ/kg.K)	Liquid Density ρ_f (kg/m^3)
101.3	60.4	112.1	1.254	1372
119.0	65.0	110.5	1.263	1359
159.6	75.0	107.0	1.283	1329
211.4	85.0	103.4	1.303	1299
275.9	95.0	99.7	1.323	1269
Vapor Density ρ_g (kg/m^3)	Liquid Viscosity μ_f (kg/m.s)	Liquid Thermal Conduct. k_f (W/m.K)	Liquid Prandtl Number Pr_f	Surface Tension σ (N/m)
9.66	0.000355	0.0619	7.19	0.0117
11.26	0.000339	0.0610	7.02	0.0114
14.94	0.000306	0.0590	6.65	0.0105
19.61	0.000279	0.0571	6.36	0.0096
25.47	0.000256	0.0551	6.13	0.0088

b

TABLE II
SPRAY NOZZLE PARAMETERS

Nozzle	d_0 (m)	θ (°)
1	0.76×10^{-3}	55.8
2	1.19×10^{-3}	46.4
3	1.70×10^{-3}	48.5

Table III shows the thermal performance results for R134a. Because of the small temperature range possible with this coolant, subcooling values range from 0 °C to only 8.9 °C. This small range is a cause for concern since spray formation requires a minimum of 10 °C to produce repeatable, fully developed droplet breakup [13]. The flow rate ranges indicated in Table III are those that were shown by Mudawar and Estes to produce fully developed droplet breakup. Overall, values of the nucleate boiling coefficient B are quite small, which corresponds to large surface-to-fluid temperature differences. A measurable increase in the magnitude of B is realized at the higher of the two saturation pressures. CHF values for this coolant are surprisingly large, exceeding the required heat flux of 200 W/cm^2. Table III shows that CHF increases with increasing flow rate, but it is slightly smaller at the higher of the two pressures. Comparing values for $\Delta T_{\rm sub} = 8.9$ °C and $\Delta T_{\rm sub} = 0$ °C at 2069 kPa shows that, while CHF does increase with subcooling, this effect is quite weak for sprays. Overall, the large CHF values for R134a may be attributed to the high pressure attainable with this coolant at relatively low coolant temperatures. However, substituting the calculated B values and $q''_s = 200$ W/cm^2 in (13) yields surface temperatures that exceed the maximum allowable temperature of 125 °C. This indicates that spray cooling with R134a may not meet the stated goals of 200 W/cm^2 while maintaining surface temperatures below 125 °C.

Table IV shows the thermal results for HFE-7100, which spans virtually the entire saturation temperature range allowed in a hybrid vehicle cooling loop. This facilitates using this coolant over a broad range of pressures, temperatures, and subcoolings, evidenced by the relatively large number of cases examined in Table IV. Overall, values of B are far greater than those for R134a, meaning *HFE-7100 can maintain far smaller device surface temperatures than R134a can*. Substituting these B values in (13) shows that this coolant can maintain device temperatures below the maximum allowable temperature of 125 °C even when dissipating 200 W/cm^2. The magnitude of B increases with increasing flow rate and decreasing pressure. Table IV shows that CHF for HFE-7100 exceeds 200 W/cm^2 at saturation temperatures of 85 °C or greater (the shaded values in Table IV). Table IV indicates that *CHF increases appreciably with increasing flow rate, but only mildly with increasing subcooling and/or pressure*.

Given the inability of R134a to maintain the required device temperatures and the positive results of HFE-7100, validation experiments were performed with the latter fluid. In the next section, we describe the experimental methods used and discuss the results of the validation study.

V. EXPERIMENTAL VALIDATION

A. Test Facility

Fig. 6 illustrates the construction of a test heater that was used to simulate chip heat dissipation to a spray. The test heater consists of a 1.0×1.0 cm^2 square surface protruding from a large cylindrical oxygen-free copper block. The test surface is surrounded with insulating G-7 fiberglass plastic. The back of the copper block is bored to accept three high-power electrical cartridge heaters. To minimize heat loss, the outer surface of the copper block is covered with high temperature ceramic insulation. The entire heater assembly is attached to a stainless steel flange for mounting to a test vessel. A thermocouple is inserted a short distance behind the square test surface, from which the surface temperature is determined. The test heater's heat flux is determined by dividing electrical power input by the square area

TABLE III
PREDICTED COOLING PERFORMANCE FOR R134a

P_{sat} (kPa)	T_{sat} (°C)	T_f (°C)	ΔT_{sub} (°C)	Q (m^3/s)			B			CHF (W/m^2)			T_s (° C) at 200 W/cm^2		
				Nozzle 1	Nozzle 2	Nozzle 3	Nozzle 1	Nozzle 2	Nozzle 3	Nozzle 1	Nozzle 2	Nozzle 3	Nozzle 1	Nozzle 2	Nozzle 3
1700	60	60	0	4.0×10^{-6}	8.0×10^{-6}	12.0×10^{-6}	2.06×10^{-6}	2.53×10^{-6}	2.84×10^{-6}	6.74×10^{6}	7.32×10^{6}	7.48×10^{6}	181.54	177.27	174.94
				6.0×10^{-6}	12.0×10^{-6}	18.0×10^{-6}	3.14×10^{-6}	3.86×10^{-6}	4.32×10^{-6}	8.19×10^{6}	8.89×10^{6}	9.08×10^{6}	172.95	168.97	166.85
				8.0×10^{-6}	16.0×10^{-6}	24.0×10^{-6}	4.23×10^{-6}	5.20×10^{-6}	5.83×10^{-6}	9.40×10^{6}	10.2×10^{6}	10.4×10^{6}	167.25	163.46	161.43
2069	68.9	60	8.9	4.0×10^{-6}	8.0×10^{-6}	12.0×10^{-6}	2.42×10^{-6}	3.00×10^{-6}	3.36×10^{-6}	6.85×10^{6}	7.44×10^{6}	7.63×10^{6}	178.18	173.85	171.63
				6.0×10^{-6}	12.0×10^{-6}	18.0×10^{-6}	3.69×10^{-6}	4.57×10^{-6}	5.12×10^{-6}	8.33×10^{6}	9.04×10^{6}	9.27×10^{6}	169.82	165.81	163.74
				8.0×10^{-6}	16.0×10^{-6}	24.0×10^{-6}	4.98×10^{-6}	6.16×10^{-6}	6.90×10^{-6}	9.57×10^{6}	10.4×10^{6}	10.6×10^{6}	164.24	160.46	158.50
		68.9	0	4.0×10^{-6}	8.0×10^{-6}	12.0×10^{-6}	2.42×10^{-6}	3.00×10^{-6}	3.36×10^{-6}	6.71×10^{6}	7.28×10^{6}	7.48×10^{6}	187.08	182.75	180.53
				6.0×10^{-6}	12.0×10^{-6}	18.0×10^{-6}	3.69×10^{-6}	4.57×10^{-6}	5.12×10^{-6}	8.16×10^{6}	8.85×10^{6}	9.08×10^{6}	178.72	174.71	172.64
				8.0×10^{-6}	16.0×10^{-6}	24.0×10^{-6}	4.98×10^{-6}	6.16×10^{-6}	6.90×10^{-6}	9.37×10^{6}	10.2×10^{6}	10.4×10^{6}	173.14	169.36	167.40

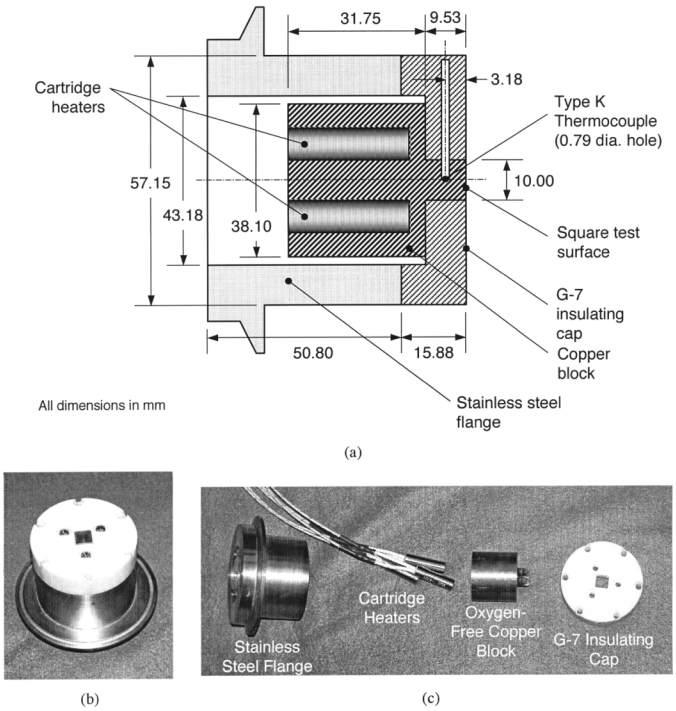

Fig. 6. (a) Construction of test heater. (b) Photo of heater assembly depicting square test surface centered in G-7 insulating cap. (c) Photos of individual test heater parts.

of the test surface. Maximum heat loss is estimated at less than 7% of the electrical power input.

Fig. 7 depicts the two-phase flow loop that is designed to deliver the test fluid at the desired pressure, temperature and flow rate to the spray nozzle located inside the loop's test chamber. The coolant is partially evaporated upon impact with the test heater. The remaining liquid accumulates in the bottom of the test vessel, while the vapor is separated from it by buoyancy into the vessel's top region. As illustrated in Fig. 7(a), liquid from the test vessel drains directly to a gear pump. The pumped liquid passes through a regulating valve followed by a plate-type heat exchanger, where the fluid is subcooled. The heat is rejected to water circulating through the plate heat exchanger. This water is supplied from a pump contained in a secondary liquid-to-air cooler with a self-contained reservoir. The heat absorbed by the water is rejected to an air-cooled finned-tube heat exchanger integral to the liquid-to-air cooler. Exiting the plate heat exchanger, the primary liquid flows through a rotameter followed by an in-line filter before returning to the spray nozzle. A separate air-cooled finned-tube heat exchanger is situated above the test vessel for deaeration purposes.

The working fluid is deaerated for about 45 min before each series of experiments. The fluid is first poured into the test vessel and the pump started to circulate the fluid through the loop. The test heater, which is located inside the test vessel, and three wrap-around test vessel heaters are then turned on. A mixture of the test fluid's vapor and air accumulates in the upper region of the test vessel; from there it is routed by buoyancy into the finned-tube heat exchanger. The vapor is recaptured by condensation as noncondensible gases are purged to the ambient. Following the deaeration process, the flow loop is sealed completely from the ambient to maintain the purity of the working fluid during the thermal tests.

All tests are performed with the spray orifice situated from the test surface according to (3), such that the spray impact area just inscribes the square test surface in order to achieve the highest possible CHF. For a given spray flow rate, the desired saturation pressure inside the test vessel as well as liquid subcooling at the nozzle inlet are achieved by simultaneously regulating heat input to the test vessel's wrap-around heaters and water flow through the plate-type heat exchanger. Boiling data are generated by supplying electrical power to the test heater's cartridge heaters in small increments that are each followed by a 30- to 40-min waiting period to allow the test surface to reach steady-state temperature. Experiments are terminated when an unsteady rise in the test heater temperature signals the commencement of CHF.

Uncertainties in the pressure, flow rate, and temperature measurements are less than 0.25%, 2.0%, and ± 0.1 °C, respectively.

B. Experimental Results

CHF was found in the previous section to increase appreciably with increasing flow rate but only mildly with increasing subcooling and/or pressure. Therefore, all the validation tests were performed with nozzle 3 (see Table III), which provides, for the same pressure drop, the largest flow rate of the three nozzles examined earlier.

TABLE IV
PREDICTED COOLING PERFORMANCE FOR HFE 7100

P_{sat} (kPa)	T_{sat} (°C)	T_f (°C)	ΔT_{sub} (°C)	Q (m^3/s)			B			CHF (W/m^2)			T_s (°C) at 200 W/cm^2		
				Nozzle 1	Nozzle 2	Nozzle 3	Nozzle 1	Nozzle 2	Nozzle 3	Nozzle 1	Nozzle 2	Nozzle 3		Nozzle 2	Nozzle 3
101.3	60.4	60	0.4	$4.0x10^{-6}$	$8.0x10^{-6}$	$12.0x10^{-6}$	$7.58x10^{-4}$	$9.32x10^{-4}$	$10.5x10^{-4}$	$1.36x10^{6}$	$1.48x10^{6}$	$1.51x10^{6}$	CHF	CHF	CHF
				$6.0x10^{-6}$	$12.0x10^{-6}$	$18.0x10^{-6}$	$11.5x10^{-4}$	$14.2x10^{-4}$	$16.0x10^{-4}$	$1.66x10^{6}$	$1.80x10^{6}$	$1.84x10^{6}$	CHF	CHF	CHF
				$8.0x10^{-6}$	$16.0x10^{-6}$	$24.0x10^{-6}$	$15.5x10^{-4}$	$19.1x10^{-4}$	$21.5x10^{-4}$	$1.90x10^{6}$	$2.06x10^{6}$	$2.11x10^{6}$	CHF	97.04	96.29
119.0	65	60	5	$4.0x10^{-6}$	$8.0x10^{-6}$	$12.0x10^{-6}$	$5.49x10^{-4}$	$6.76x10^{-4}$	$7.58x10^{-4}$	$1.52x10^{6}$	$1.65x10^{6}$	$1.68x10^{6}$	CHF	CHF	CHF
				$6.0x10^{-6}$	$12.0x10^{-6}$	$18.0x10^{-6}$	$8.36x10^{-4}$	$10.3x10^{-4}$	$11.5x10^{-4}$	$1.84x10^{6}$	$2.01x10^{6}$	$2.05x10^{6}$	CHF	101.24	100.46
				$8.0x10^{-6}$	$16.0x10^{-6}$	$24.0x10^{-6}$	$11.3x10^{-4}$	$13.9x10^{-4}$	$15.5x10^{-4}$	$2.12x10^{6}$	$2.30x10^{6}$	$2.35x10^{6}$	100.58	99.15	98.41
		65	0	$4.0x10^{-6}$	$8.0x10^{-6}$	$12.0x10^{-6}$	$5.49x10^{-4}$	$6.76x10^{-4}$	$7.58x10^{-4}$	$1.50x10^{6}$	$1.63x10^{6}$	$1.66x10^{6}$	CHF	CHF	CHF
				$6.0x10^{-6}$	$12.0x10^{-6}$	$18.0x10^{-6}$	$8.36x10^{-4}$	$10.3x10^{-4}$	$11.5x10^{-4}$	$1.82x10^{6}$	$1.98x10^{6}$	$2.02x10^{6}$	CHF	CHF	105.46
				$8.0x10^{-6}$	$16.0x10^{-6}$	$24.0x10^{-6}$	$11.3x10^{-4}$	$13.9x10^{-4}$	$15.5x10^{-4}$	$2.09x10^{6}$	$2.27x10^{6}$	$2.32x10^{6}$	105.58	104.15	103.41
159.6	75	60	15	$4.0x10^{-6}$	$8.0x10^{-6}$	$12.0x10^{-6}$	$3.14x10^{-4}$	$3.88x10^{-4}$	$4.35x10^{-4}$	$1.81x10^{6}$	$1.98x10^{6}$	$2.02x10^{6}$	CHF	CHF	107.91
				$6.0x10^{-6}$	$12.0x10^{-6}$	$18.0x10^{-6}$	$4.79x10^{-4}$	$5.90x10^{-4}$	$6.62x10^{-4}$	$2.20x10^{6}$	$2.40x10^{6}$	$2.45x10^{6}$	107.12	105.44	104.54
				$8.0x10^{-6}$	$16.0x10^{-6}$	$24.0x10^{-6}$	$6.45x10^{-4}$	$7.95x10^{-4}$	$8.92x10^{-4}$	$2.54x10^{6}$	$2.75x10^{6}$	$2.81x10^{6}$	104.74	103.14	102.29
		65	10	$4.0x10^{-6}$	$8.0x10^{-6}$	$12.0x10^{-6}$	$3.14x10^{-4}$	$3.88x10^{-4}$	$4.35x10^{-4}$	$1.80x10^{6}$	$1.96x10^{6}$	$2.00x10^{6}$	CHF	CHF	112.91
				$6.0x10^{-6}$	$12.0x10^{-6}$	$18.0x10^{-6}$	$4.79x10^{-4}$	$5.90x10^{-4}$	$6.62x10^{-4}$	$2.18x10^{6}$	$2.38x10^{6}$	$2.43x10^{6}$	112.12	110.44	109.54
				$8.0x10^{-6}$	$16.0x10^{-6}$	$24.0x10^{-6}$	$6.45x10^{-4}$	$7.95x10^{-4}$	$8.92x10^{-4}$	$2.51x10^{6}$	$2.72x10^{6}$	$2.78x10^{6}$	109.74	108.14	107.29
		75	0	$4.0x10^{-6}$	$8.0x10^{-6}$	$12.0x10^{-6}$	$3.14x10^{-4}$	$3.88x10^{-4}$	$4.35x10^{-4}$	$1.76x10^{6}$	$1.92x10^{6}$	$1.96x10^{6}$	CHF	CHF	CHF
				$6.0x10^{-6}$	$12.0x10^{-6}$	$18.0x10^{-6}$	$4.79x10^{-4}$	$5.90x10^{-4}$	$6.62x10^{-4}$	$2.14x10^{6}$	$2.33x10^{6}$	$2.38x10^{6}$	122.12	120.44	119.54
				$8.0x10^{-6}$	$16.0x10^{-6}$	$24.0x10^{-6}$	$6.45x10^{-4}$	$7.95x10^{-4}$	$8.92x10^{-4}$	$2.46x10^{6}$	$2.67x10^{6}$	$2.73x10^{6}$	119.74	118.14	117.29
211.4	85	60	25	$4.0x10^{-6}$	$8.0x10^{-6}$	$12.0x10^{-6}$	$1.89x10^{-4}$	$2.33x10^{-4}$	$2.60x10^{-4}$	$2.12x10^{6}$	$2.31x10^{6}$	$2.36x10^{6}$	115.39	113.41	112.40
				$6.0x10^{-6}$	$12.0x10^{-6}$	$18.0x10^{-6}$	$2.88x10^{-4}$	$3.54x10^{-4}$	$3.96x10^{-4}$	$2.58x10^{6}$	$2.81x10^{6}$	$2.87x10^{6}$	111.47	109.66	108.70
				$8.0x10^{-6}$	$16.0x10^{-6}$	$24.0x10^{-6}$	$3.88x10^{-4}$	$4.77x10^{-4}$	$5.34x10^{-4}$	$2.96x10^{6}$	$3.22x10^{6}$	$3.30x10^{6}$	108.87	107.15	106.23
		65	20	$4.0x10^{-6}$	$8.0x10^{-6}$	$12.0x10^{-6}$	$1.89x10^{-4}$	$2.33x10^{-4}$	$2.60x10^{-4}$	$2.10x10^{6}$	$2.29x10^{6}$	$2.34x10^{6}$	120.39	118.41	117.40
				$6.0x10^{-6}$	$12.0x10^{-6}$	$18.0x10^{-6}$	$2.88x10^{-4}$	$3.54x10^{-4}$	$3.96x10^{-4}$	$2.56x10^{6}$	$2.79x10^{6}$	$2.85x10^{6}$	116.47	114.66	113.70
				$8.0x10^{-6}$	$16.0x10^{-6}$	$24.0x10^{-6}$	$3.88x10^{-4}$	$4.77x10^{-4}$	$5.34x10^{-4}$	$2.94x10^{6}$	$3.20x10^{6}$	$3.27x10^{6}$	113.87	112.15	111.23
		75	10	$4.0x10^{-6}$	$8.0x10^{-6}$	$12.0x10^{-6}$	$1.89x10^{-4}$	$2.33x10^{-4}$	$2.60x10^{-4}$	$2.07x10^{6}$	$2.26x10^{6}$	$2.31x10^{6}$	130.39	128.41	127.40
				$6.0x10^{-6}$	$12.0x10^{-6}$	$18.0x10^{-6}$	$2.88x10^{-4}$	$3.54x10^{-4}$	$3.96x10^{-4}$	$2.52x10^{6}$	$2.74x10^{6}$	$2.80x10^{6}$	126.47	124.66	123.70
				$8.0x10^{-6}$	$16.0x10^{-6}$	$24.0x10^{-6}$	$3.88x10^{-4}$	$4.77x10^{-4}$	$5.34x10^{-4}$	$2.90x10^{6}$	$3.15x10^{6}$	$3.22x10^{6}$	123.87	122.15	121.23
		85	0	$4.0x10^{-6}$	$8.0x10^{-6}$	$12.0x10^{-6}$	$1.89x10^{-4}$	$2.33x10^{-4}$	$2.60x10^{-4}$	$2.04x10^{6}$	$2.22x10^{6}$	$2.27x10^{6}$	140.39	138.41	137.40
				$6.0x10^{-6}$	$12.0x10^{-6}$	$18.0x10^{-6}$	$2.88x10^{-4}$	$3.54x10^{-4}$	$3.96x10^{-4}$	$2.48x10^{6}$	$2.70x10^{6}$	$2.76x10^{6}$	136.47	134.66	133.70
				$8.0x10^{-6}$	$16.0x10^{-6}$	$24.0x10^{-6}$	$3.88x10^{-4}$	$4.77x10^{-4}$	$5.34x10^{-4}$	$2.85x10^{6}$	$3.10x10^{6}$	$3.17x10^{6}$	133.87	132.15	131.23
275.9	95	60	35	$4.0x10^{-6}$	$8.0x10^{-6}$	$12.0x10^{-6}$	$1.18x10^{-4}$	$1.45x10^{-4}$	$1.63x10^{-4}$	$2.45x10^{6}$	$2.67x10^{6}$	$2.72x10^{6}$	120.11	118.00	116.83
				$6.0x10^{-6}$	$12.0x10^{-6}$	$18.0x10^{-6}$	$1.79x10^{-4}$	$2.20x10^{-4}$	$2.48x10^{-4}$	$2.98x10^{6}$	$3.25x10^{6}$	$3.32x10^{6}$	115.91	113.94	112.83
				$8.0x10^{-6}$	$16.0x10^{-6}$	$24.0x10^{-6}$	$2.42x10^{-4}$	$2.97x10^{-4}$	$3.34x10^{-4}$	$3.42x10^{6}$	$3.73x10^{6}$	$3.81x10^{6}$	113.06	111.20	110.16
		65	30	$4.0x10^{-6}$	$8.0x10^{-6}$	$12.0x10^{-6}$	$1.18x10^{-4}$	$1.45x10^{-4}$	$1.63x10^{-4}$	$2.44x10^{6}$	$2.66x10^{6}$	$2.71x10^{6}$	125.11	123.00	121.83
				$6.0x10^{-6}$	$12.0x10^{-6}$	$18.0x10^{-6}$	$1.79x10^{-4}$	$2.20x10^{-4}$	$2.48x10^{-4}$	$2.97x10^{6}$	$3.23x10^{6}$	$3.30x10^{6}$	120.91	118.94	117.83
				$8.0x10^{-6}$	$16.0x10^{-6}$	$24.0x10^{-6}$	$2.42x10^{-4}$	$2.97x10^{-4}$	$3.34x10^{-4}$	$3.40x10^{6}$	$3.70x10^{6}$	$3.79x10^{6}$	118.06	116.20	115.16
		75	20	$4.0x10^{-6}$	$8.0x10^{-6}$	$12.0x10^{-6}$	$1.18x10^{-4}$	$1.45x10^{-4}$	$1.63x10^{-4}$	$2.41x10^{6}$	$2.62x10^{6}$	$2.68x10^{6}$	135.11	133.00	131.83
				$6.0x10^{-6}$	$12.0x10^{-6}$	$18.0x10^{-6}$	$1.79x10^{-4}$	$2.20x10^{-4}$	$2.48x10^{-4}$	$2.93x10^{6}$	$3.19x10^{6}$	$3.26x10^{6}$	130.91	128.94	127.83
				$8.0x10^{-6}$	$16.0x10^{-6}$	$24.0x10^{-6}$	$2.42x10^{-4}$	$2.97x10^{-4}$	$3.34x10^{-4}$	$3.36x10^{6}$	$3.66x10^{6}$	$3.74x10^{6}$	128.06	126.20	125.16
		85	10	$4.0x10^{-6}$	$8.0x10^{-6}$	$12.0x10^{-6}$	$1.18x10^{-4}$	$1.45x10^{-4}$	$1.63x10^{-4}$	$2.38x10^{6}$	$2.59x10^{6}$	$2.64x10^{6}$	145.11	143.00	141.83
				$6.0x10^{-6}$	$12.0x10^{-6}$	$18.0x10^{-6}$	$1.79x10^{-4}$	$2.20x10^{-4}$	$2.48x10^{-4}$	$2.90x10^{6}$	$3.15x10^{6}$	$3.22x10^{6}$	140.91	138.94	137.83
				$8.0x10^{-6}$	$16.0x10^{-6}$	$24.0x10^{-6}$	$2.42x10^{-4}$	$2.97x10^{-4}$	$3.34x10^{-4}$	$3.32x10^{6}$	$3.62x10^{6}$	$3.70x10^{6}$	138.06	136.20	135.16
		95	0	$4.0x10^{-6}$	$8.0x10^{-6}$	$12.0x10^{-6}$	$1.18x10^{-4}$	$1.45x10^{-4}$	$1.63x10^{-4}$	$2.35x10^{6}$	$2.56x10^{6}$	$2.61x10^{6}$	155.11	153.00	151.83
				$6.0x10^{-6}$	$12.0x10^{-6}$	$18.0x10^{-6}$	$1.79x10^{-4}$	$2.20x10^{-4}$	$2.48x10^{-4}$	$2.86x10^{6}$	$3.11x10^{6}$	$3.18x10^{6}$	150.91	148.94	147.83
				$8.0x10^{-6}$	$16.0x10^{-6}$	$24.0x10^{-6}$	$2.42x10^{-4}$	$2.97x10^{-4}$	$3.34x10^{-4}$	$3.28x10^{6}$	$3.57x10^{6}$	$3.65x10^{6}$	148.06	146.20	145.16

Fig. 8 shows boiling curves obtained for nozzle 3 at different flow rates, pressures, and subcoolings. The tested range for each of these parameters is broken into *high*, *medium*, and *low* subranges. Note that the boiling curves tend to cluster in the nucleate boiling region. Large variations in CHF are primarily the result of flow rate variations and, to a far lesser extent, subcooling or pressure variations. In fact, all four *high* flow rate cases successfully meet the hybrid vehicle cooling requirements. Notice how CHF values for these cases exceed 200 W/cm^2 at surface temperatures safely below 125 °C. On the other hand, *medium* and *low* flow rates fail to reach the 200 W/cm^2 level, although surface temperatures at CHF for these cases are below 125 °C.

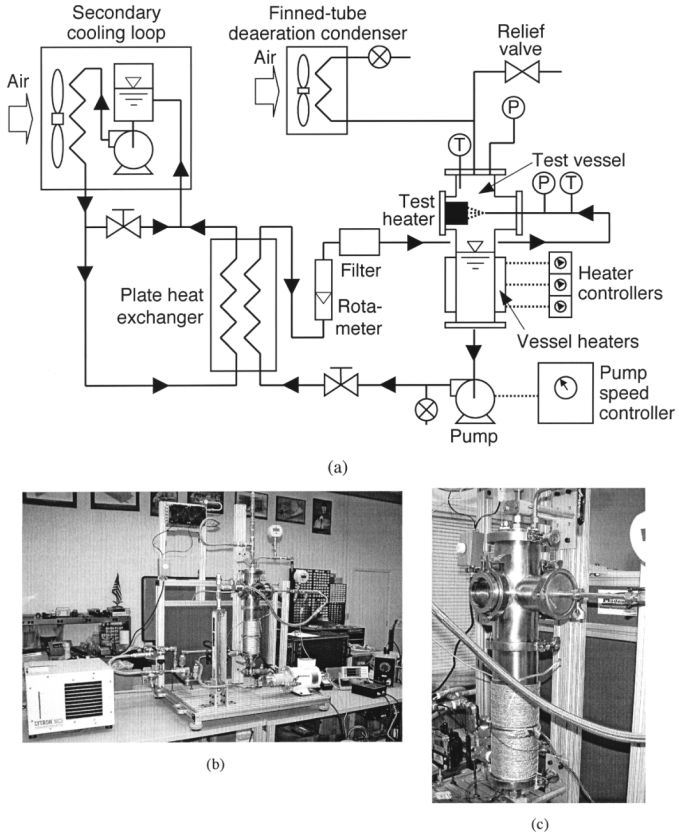

Fig. 7. (a) Schematic of flow loop. (b) Photo of test facility. (c) Photo of test vessel.

Fig. 9 compares measured and predicted CHF for all the validation tests. Overall, the data are slightly higher than predicted, but trends relative to flow rate, subcooling, and pressure appear to be correctly captured.

These findings demonstrate that spray cooling is a viable approach that can meet the stringent thermal management requirements of hybrid vehicles.

VI. Summary and Conclusion

This paper explored thermal management solutions for high-flux electronics in hybrid vehicles. Different cooling systems were considered along with a comprehensive assessment of the suitability of different refrigerants and liquid coolants to this application. Recent models were reviewed and integrated into a systematic methodology for predicting the cooling performance of pressure spray nozzles. This methodology was used to explore the effectiveness of two-phase sprays and identify an optimum coolant. It also identifies desired ranges of spray parameters that could safely dissipate 150–200 W/cm^2 while maintaining the chip temperature below 125 °C. Finally, those predictions were validated experimentally. The key conclusions of this study are as follows.

1) Different refrigerants and liquid coolants were assessed relative to the desired pressure–temperature operation envelope for hybrid vehicle electronics. This also included evaluating the coolants' environmental impact, dielectric properties, safety, and material compatibility, as well as determining the availability of detailed thermophysical property data. Only hydrofluorocarbons (HFCs) scored well in all these performance categories. Of the HFCs, one refrigerant, R134a, and one liquid coolant, HFE-7100, show the greatest promise.
2) The predictive methodology for two-phase spray cooling shows that R134a can yield CHF values that greatly exceed the heat fluxes anticipated in hybrid vehicle electronics. However, this coolant is not capable of maintaining device temperatures below the maximum allowable temperature of 125 °C when dissipating 200 W/cm^2. With HFE-7100,

	Test #	Flow Rate	Pressure	Subcooling	CHF
◇	1	High (1.305×10^{-5} m^3/s) (0.207 gpm)	Low (1.44×10^5 N/m^2) (20.9 psia)	High (38.5 °C)	263 W/cm^2
⧖	2	High (1.305×10^{-5} m^3/s) (0.207 gpm)	Medium (1.71×10^5 N/m^2) (24.8 psia)	Low (24.6 °C)	205 W/cm^2 at 105.8 °C
▽	3	High (1.160×10^{-5} m^3/s) (0.184 gpm)	Low (1.36×10^5 N/m^2) (19.7 psia)	High (36.8 °C)	245 W/cm^2 at 110.4 °C
□	4	Medium (0.725×10^{-5} m^3/s) (0.115 gpm)	Low (1.36×10^5 N/m^2) (19.7 psia)	High (39.2 °C)	194 W/cm^2 at 104.1 °C
⋈	5	High (1.160×10^{-5} m^3/s) (0.184 gpm)	Medium (1.64×10^5 N/m^2) (23.8 psia)	High (41.9 °C)	----
△	6	High (1.051×10^{-5} m^3/s) (0.167 gpm)	Medium (1.77×10^5 N/m^2) (25.6 psia)	High (43.0 °C)	255 W/cm^2 at 109.6 °C
○	7	Low (0.353×10^{-5} m^3/s) (0.056 gpm)	High (2.14×10^5 N/m^2) (31.3 psia)	High (56.1 °C)	175 W/cm^2 at 116.0 °C
⊗	8	Low (0.372×10^{-5} m^3/s) (0.059 gpm)	Low (1.42×10^5 N/m^2) (17.8 psia)	High (40.6 °C)	138 W/cm^2 at 97.9 °C

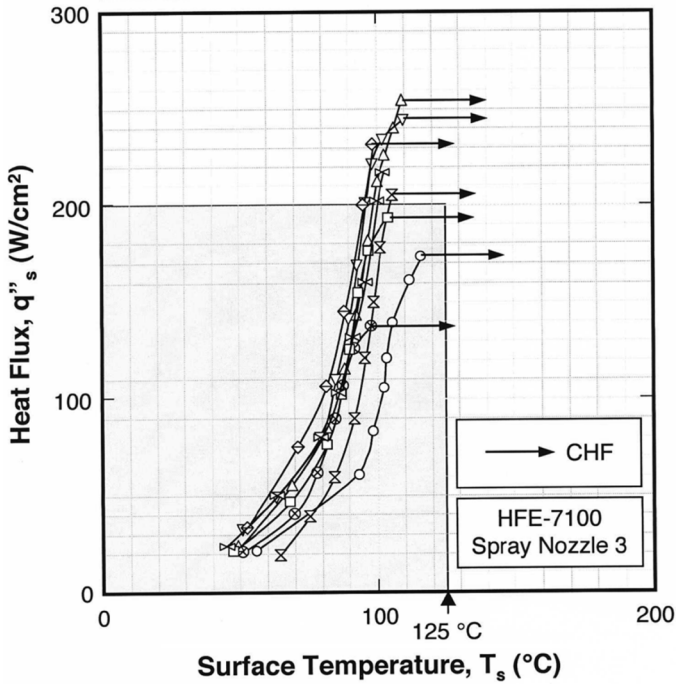

Fig. 8. Boiling curves from thermal tests.

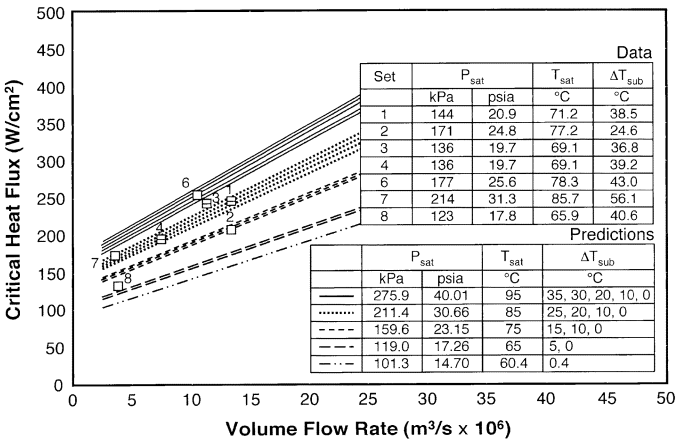

Set	P_{sat}		T_{sat}	ΔT_{sub}
	kPa	psia	°C	°C
1	144	20.9	71.2	38.5
2	171	24.8	77.2	24.6
3	136	19.7	69.1	36.8
4	136	19.7	69.1	39.2
6	177	25.6	78.3	43.0
7	214	31.3	85.7	56.1
8	123	17.8	65.9	40.6

	P_{sat}		T_{sat}	ΔT_{sub}
	kPa	psia	°C	°C
——	275.9	40.01	95	35, 30, 20, 10, 0
·····	211.4	30.66	85	25, 20, 10, 0
- - - -	159.6	23.15	75	15, 10, 0
— —	119.0	17.26	65	5, 0
— ··· —	101.3	14.70	60.4	0.4

Fig. 9. Comparison of CHF predictions and experimental data.

several operating conditions were identified that yield CHF values in excess of 200 W/cm^2 and surface temperatures below 125 °C.

3) The attractive performance of HFE-7100 was validated experimentally for different flow rates, subcoolings and pressures. These tests prove that CHF is sensitive primarily to flow rate and, to a far lesser extent, subcooling and pressure. High flow rate tests exceed the 200 W/cm^2 heat flux requirement at surface temperatures safely below 125 °C. These findings demonstrate the viability of HFE-7100 spray cooling in terms of meeting the thermal management requirements of hybrid vehicles.

REFERENCES

[1] "Electrical and electronics technical team roadmap," Electrical and Electronics Technical Team, U.S. Dept. of Energy, Washington, DC, 2006.

[2] K. Bennion, "Plug-in hybrid electric vehicle impacts on power electronics and electric machines," National Renewable Energy Lab., Golden, CO, NREL Tech. Rep. NREL/MP-540-36085, 2007.

[3] I. Mudawar, "Assessment of high-heat-flux thermal management schemes," *IEEE Trans. Compon. Packag. Technol.*, vol. 24, no. 2, pp. 122–141, Jun. 2001.

[4] S. Toda, "A study in mist cooling (1st report: Investigation of mist cooling)," *Trans. JSME*, vol. 38, pp. 581–588, 1972.

[5] M. Monde, "Critical heat flux in saturated forced convection boiling with an impinging droplet," *Trans. JSME*, vol. 46, pp. 1146–1155, 1980.

[6] C. S. K. Cho and K. Wu, "Comparison of burnout characteristics in jet impingement cooling and spray cooling," in *Proc. Nat. Heat Transfer Conf.*, Houston, TX, 1988, pp. 561–567.

[7] I. Mudawar and W. S. Valentine, "Determination of the local quench curve for spray-cooled metallic surfaces," *J. Heat Treating*, vol. 7, pp. 107–121, 1989.

[8] K. A. Estes and I. Mudawar, "Correlation of Sauter mean diameter and critical heat flux for spray cooling of small surfaces," *Int. J. Heat Mass Transfer*, vol. 38, pp. 2985–2996, 1995.

[9] R.-H. Chen, L. C. Chow, and J. E. Navedo, "Effects of spray characteristics on critical heat flux in subcooled water spray cooling," *Int. J. Heat Mass Transfer*, vol. 45, pp. 4033–4043, 2002.

[10] D. D. Hall and I. Mudawar, "Experimental and numerical study of quenching complex-shaped metallic alloys with multiple, overlapping sprays," *Int. J. Heat Mass Transfer*, vol. 38, pp. 1201–1216, 1995.

[11] I. Mudawar, "Spray cooling of power electronics," Subcontract report to the National Renewable Energy Laboratory, West Lafayette, IN, 2006.

[12] I. H. Rowlands, "The fourth meeting of the parties to the Montreal Protocol: Report and reflection," *Environment*, vol. 35, pp. 25–34, 1993.

[13] I. Mudawar and K. A. Estes, "Optimizing and predicting CHF in spray cooling of a square surface," *J. Heat Transfer*, vol. 118, pp. 672–680, 1996.

[14] J. R. Rybicki and I. Mudawar, "Single-phase and two-phase cooling characteristics of upward-facing and downward-facing sprays," *Int. J. Heat Mass Transfer*, vol. 49, pp. 5–12, 2006.

Issam Mudawar received the M.S. and Ph.D. degrees from the Massachusetts Institute of Technology, Cambridge, in 1980 and 1984, respectively. His graduate work involved magnetohydrodynamic (MHD) energy conversion and phase-change water cooling of turbine blades.

He joined the Purdue University School of Mechanical Engineering, West Lafayette, IN, in 1984, where he established, and became Director of, the Boiling and Two-Phase Flow Laboratory (BTPFL) and Purdue University International Electronic Alliance (PUIECA). His work has been focused on phase change processes, thermal management of electronic and aerospace devices, intelligent materials processing, hydrogen storage, high-Mach turbine engines, and nuclear reactor safety. His theoretical and experimental research encompasses sensible and evaporative heating of thin films, pool boiling, flow boiling, jet-impingement cooling, spray cooling, microchannel heat sinks, heat transfer enhancement, heat transfer in rotating systems, critical heat flux, and capillary pumped flows. He is also President of Mudawar Thermal Systems, Inc., a firm that is dedicated to the development of thermal management solutions.

Prof. Mudawar received several awards for his research accomplishments, including Best Paper Award in Electronic Cooling at the 1988 National Heat Transfer Conference, Best Paper Award in Thermal Management at the 1992 ASME/JSME Joint Conference on Electronic Packaging, the *Journal of Electronic Packaging* Outstanding Paper of the Year Award for 1995, and the Best Paper Award in Thermal Management at ITherm 2008. He also received several awards for excellence in teaching and service to Purdue students and their organizations, including the Solberg Award for Best Teacher in School of Mechanical Engineering (1987, 1992, 1996, 2004), the Charles Murphy Award for Best Teacher at Purdue University (1997), and the National Society of Black Engineers Professor of the Year Award (1985, 1987). He was named Fellow of the American Society of Mechanical Engineers (ASME) in 1998.

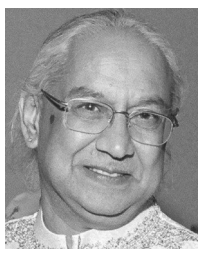

Desikan Bharathan received the B.Tech. degree from the Indian Institute of Technology, Madras, in 1970 and the M.S. and Ph.D. degrees from the University of Virginia, Charlottesville, in 1972 and 1976, all in aerospace engineering.

He joined the National Renewable Energy Laboratory (NREL), Golden, CO, in 1980, and is currently a Principal Engineer. At NREL, over the past 28 years, he has worked on ocean thermal energy, building cooling, wind energy, geothermal, and is currently working in the transportation group. He has published several articles and chapters in books, and holds five patents in various areas.

Dr. Bharathan received two R&D 100 Awards for innovations in evaporation and condensation at low temperatures and pressures. He is a member of AIChE and a fellow of the ASME.

Kenneth Kelly received the B.S. and M.S. degrees in mechanical engineering from Ohio University, Columbus, in 1986 and 1989, respectively.

He joined the National Renewable Energy Laboratory (NREL) in 1991 and is a Senior Engineer. He is also currently the Task Leader for research and development of advanced thermal control technologies for automotive power electronics. Previously, he led efforts in Robust Design—for fuel cells and advanced heavy-duty hybrid electric vehicles. He also has experience with alternative-fuel vehicle emissions testing and fleet evaluations. He worked in industry as a Manufacturing Engineering with Swagelok Company.

Sreekant Narumanchi (M'06) received the B.Tech. degree from the Indian Institute of Technology, Kanpur, in 1997, the M.S. degree from Washington State University, Pullman, in 1999, and the Ph.D. degree from Carnegie Mellon University, Pittsburgh, PA, in 2003, all in mechanical engineering. His Ph.D. work involved development of novel models for heat conduction at micro/nanoscales for microelectronics applications.

He joined the National Renewable Energy Laboratory (NREL), Golden, CO, in 2004, where he is currently a Senior Engineer with the Advanced Vehicle Group. His research interests include heat transfer (including micro/nanoscale heat transfer), fluid dynamics, computational fluid dynamics, electronics cooling, hybrid electric vehicles, and fuel cells. His primary assignment is with the Power Electronics task and he is exploring novel thermal control schemes for insulated gate bipolar transistor (IGBT) packages in inverters of hybrid electric vehicles. He is working on the use of liquid jets and sprays for cooling, as well as on advanced thermal interface materials. He has authored more than 30 peer-reviewed articles in journals and conferences, and one book chapter. He also serves as a reviewer/panelist for several journals and conferences, Department of Energy, and the National Science Foundation.

Dr. Narumanchi received the Best Paper Award from the *ASME Journal of Electronic Packaging* (2003), as well as the NREL Director's Award (2007). He was recently awarded a NREL Lab-Directed Research and Development Award (2008) for understanding interfacial heat transport between nanostructures and substrates via atomistic computations. He is a member of the ASME, SAE, and Sigma Xi.